Attached cavitation in a laminar separation bubble

Florent Ravelet, Amélie Danlos, Kilian Croci, Sofiane Khelladi

Attached cavitation in a laminar separation bubble

F. Ravelet, A. Danlos, K. Croci and S. Khelladi

Arts et Metiers Institute of Technology, CNAM, LIFSE, HESAM University, 75013 Paris, France

E-mail: florent.ravelet@ensam.eu

Abstract.

The present study aims at studying the inception, the growth and the potential unsteady dynamics of attached vapour cavities in large laminar separation bubbles. A viscous silicon oil has been used in a venturi geometry in order to explore the flow for Reynolds numbers ranging from $Re = 800$ to $Re = 2000$. The results show that at low Reynolds number the attached sheets that are attributed to cavitation do not have any obvious dynamics and abruptly transit to supercavitation when lowering the cavitation number. For $Re \simeq 1200$, cavitating vortices are intermittently observed in the wake of the attached cavity with no clear period. Finally, a periodic shedding/shrinking of the main cavity is first observed for $Re \gtrsim 1400$, in a narrow range of cavitation numbers, together with a slower growth of the cavities when lowering the cavitation number. This regime is then present at higher Reynolds numbers, in a wider range of cavitation numbers.

Attached sheet cavitation has been extensively studied in water turbulent flows. The presence of small separation bubbles close to the leading edge of a profile or to the summit of a wedge provides favourable conditions for the attachment of vaporous cavities when lowering the absolute pressure. The fundamentals of sheet cavitation inception can be found for instance in the classical book of J.-P. Franc [1]. The inception of such "sheet" cavitation has been for instance studied in Refs. [2, 3, 4, 5, 6] on smooth axi-symmetric bodies, on propellers blades or on foils. Moreover, a recent review on the different sheet cavitation inception mechanisms can be found in Ref. [7].

For lower pressures, the cavities usually grow and become unstable, leading to periodicall cloud shedding [8]. These instabilities are attributed to two main phenomena: the formation of a re-entrant jet which is governed by inertia [9], and a bubbly shock propagation mechanism [10]. These two mechanisms have been widely studied, at least for very large Reynolds numbers.

The current studies that are conducted in the LIFSE laboratory deal with multiphase separated flows at very low Reynolds numbers. As a first step [11, 12], the main features of the multiphase structures that arise have been observed. Single-phase numerical simulations have been performed additionally to illustrate the flow topology and to estimate the threshold for cavitation inception. With silicon oil saturated with air at atmospherice pressure, different types of cavities are observed: tadpoles that attach on the lateral wall [11], sheets that attach on the venturi slope and top-tadpoles that attach on the opposite side of the vein. The numerical simulations, pressure measurements and high-speed visualizations suggest to attribute the tadpoles to degassing, the main cavity sheet to cavitation, and the top-tadpoles to a secondary flow separation that captures air [12].

In this Article, experiments are performed for a degassed oil, in order to obtain only central attached cavities and to study their development and their stability.

1. Experimental setup

1.1. Description of the test-bench and of the protocol

The experiments are conducted in a test-bench of the *LIFSE* facilities especially designed to study cavitation in silicon oils (see Fig. 1). A *Pollard MPLN* 142 volumetric pump *(1)* impels the silicon oil in the loop. A tank of 100 liters *(2)* is equipped with a temperature sensor *ThermoEst PT100 (3)*. The tank is connected to compressed air supply or to a vacuum pump *(4)*. The oil then flows in a 40 mm inner diameter pipe and through an ultrasonic flowmeter *KHRONE Optisonic 3400 (5)* placed 1.5 m upstream of the test section *(7)*. The inlet and outlet pressures are monitored with two pressure sensors *(6)*.

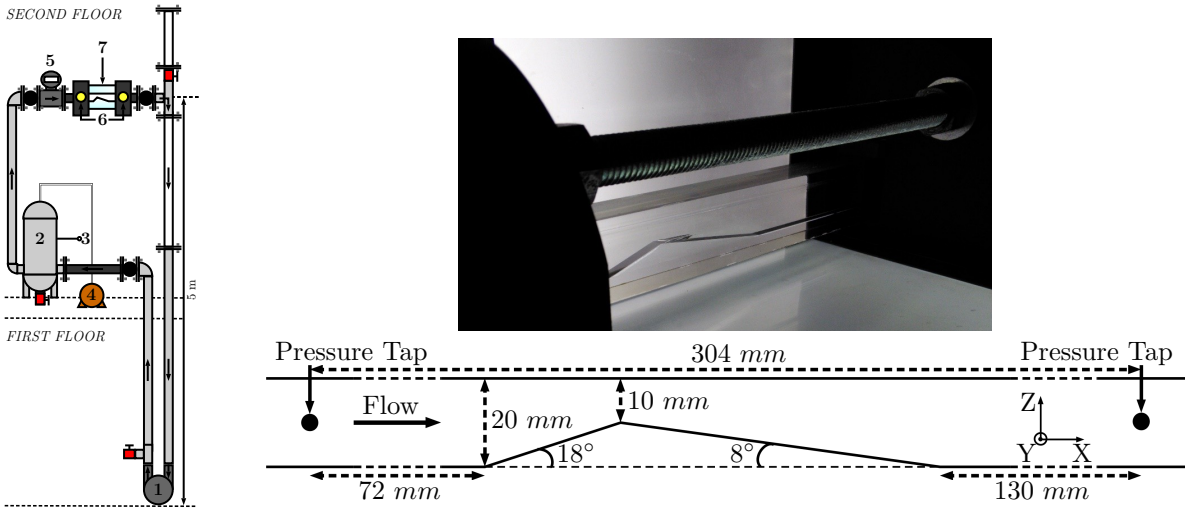

Figure 1. Sketch of the test loop with *(1)* the pump, *(2)* the oil tank, *(3)* the temperature sensor, *(4)* the compressor or vacuum pump, *(5)* the ultrasonic flowmeter, *(6)* the pressure sensors and *(7)* the operating test section. Picture and main dimensions of the test section

The test section consists of a Venturi geometry with convergent/divergent angles of respectively 18° and 8° [13]. It presents an inlet section $S_{in} = 20 \times 10$ mm^2 and a square section at the throat $S_{throat} = 10 \times 10$ mm^2. Both side and top visualizations are possible. Two round-to-rectangle contraction nozzles with an area ratio of 6.3 are placed on each sides of the test section to connect it to the pipe system.

All experiments are realized following a protocol in order to eliminate a maximum of dissolved air. The pressure in the set-up is first decreased to an absolute pressure of $\simeq 70$ mbar, then the oil is kept circulating for this pressure at slow velocity during two hours hours, while removing periodically the air that accumulates in the vertical tube situated above the outlet of the test section and visible on the top part of the sketch in Fig. 1. The measurements are then operated at roughly constant Reynolds number, increasing progressively the pressure in the test-bench.

1.2. Control parameters and flow visualization

The inlet and outlet test section pressure, named P_1 and P_2, are measured with pressure taps located respectively at 103 *mm* upstream and 201 *mm* downstream of the Venturi throat. The inlet velocity V_{in} at S_{in} is estimated from flowrate measurements. The height of the venturi inlet section $h_{in} = 20$ mm is chosen as the reference length scale for the Reynolds number. The

height of the venturi throat is $h_{throat} = 10$ mm. The viscosity and density have been measured as a function of the temperature.

Table 1. Flow parameters, ranges and estimated uncertainties for silicone oil $47V50$. The surface tension is $S \simeq 20$ mN.m^{-1} and the vapor pressure is $P_v \simeq 1.3$ Pa according to the oil data file

Symbol	Parameters	Definition	Range ($47V50$)	Unit	Uncertainty
V_{in}	Inlet velocity		$[2.12; 5.68]$	$m.s^{-1}$	$< 1\%$
T	Operating temperature		$[18.0; 22.0]$	$°C$	$< 1\%$
P_1	Inlet pressure		$[146; 708]$	$mbar$	$< 1\%$
P_2	Outlet pressure		$[2; 294]$	$mbar$	$< 1\%$
ρ	Oil density		$[961; 963]$	$kg.m^{-3}$	$< 1\%$
ν	Oil kinematic viscosity		$[52.5; 56.9]$	$mm^2.s^{-1}$	$\pm$ 2%
Re	Inlet Reynolds number	$\frac{V_{in} h_{in}}{\nu}$	$[797; 2056]$		$\pm$ 3%
σ_1	Inlet cavitation number	$\frac{P_1 - P_v}{\frac{1}{2}\rho V_{in}^2}$	$[4.42; 7.61]$		$\pm$ 4%
σ_2	Outlet cavitation number	$\frac{P_2 - P_v}{\frac{1}{2}\rho V_{in}^2}$	$[0.02; 3.50]$		$\pm$ 4%
K_p	Pressure loss coefficient	$\frac{P_1 - P_2}{\frac{1}{2}\rho V_{in}^2}$			$\pm$ 5%
Ca	Capillary number	$\frac{\rho \nu V_{in}}{S}$	$[5.4; 15.1]$		$\pm$ 4%

The following dimensionless numbers are defined based on these values: a Reynolds number, an inlet and an outlet cavitation numbers and a capillary number. The definition of these parameters, together with the ranges that have been explored in the present Article, can be found in Tab. 1. Please note that the outlet cavitation number has not been considered in the previous study [12]. It is used in the present Article as it seems to be more significant for analysing the results.

2. Results

2.1. Cavitation inception and main features of the observed structures

The topology of the single-phase flow and its nature as a function of the Reynolds number have been studied numerically [12]. The main results are plotted in Fig. 2. The experimental (obtained in single-phse flows) and numerical pressure loss coefficient fairly collapse, which is a clue in favor of the quality of the simulations. The flow remains laminar for $Re \lesssim 2000$. A primary flow separation is present in the wake of the throat, on the divergent wall ($X^* > 0$ and $Z^* < 0$), first along each lateral wall ($Y^* \simeq \pm 0.5$) for $Re \geqslant 350$, and on all along the width for $Re \geqslant 650$. This corresponds to the negative values of the velocity profile in Fig. 2. A secondary laminar boundary layer separation emerges at a Reynolds number $Re \geqslant 1100$ at the top wall of the test section ($X^* > 0$ and $Z^* \simeq 1$). Finally, the critical cavitation numbers that lead to a minimal absolute pressure equal to the vapour pressure can be estimated numerically with the simulations. For instance, here, for $Re = 1200$, $\sigma_1 = 6.57$ and $\sigma_2 = 2.58$, one can notice that the minimal pressure is close to zero and that this occurs at the throat, on the bottom wall.

Using silicon oil saturated with air at 1 bar, three types of gaseous/vaporous structures have been observed [12]. The first one is called "bottom tadpoles". They attach to the side walls close to the throat, for $Re \leqslant 650$ and at inlet pressure well above the estimated critical value

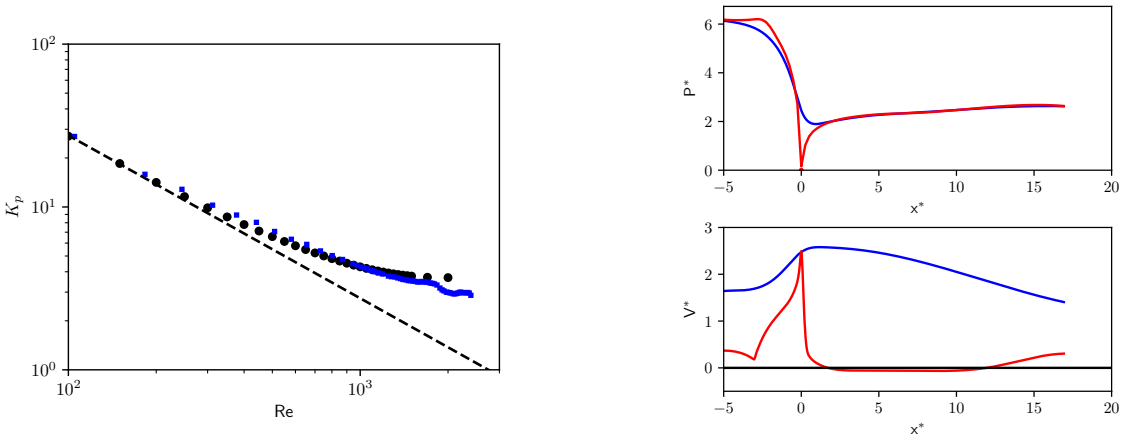

Figure 2. Left: pressure loss coefficient K_p as a function of the Reynolds number Re. Blue squares: experiments in single-phase flow and black bullets: numerical simulations. Top right: dimensionless pressure profile $P^* = P/\frac{1}{2}\rho V_{in}^2$ with respect to axial coordinate $X^* = X/h_{throat}$. Bottom right: dimensionless velocity profile $V^* = V/V_{in}$ with respect to X^*. Data for $Re = 1200$, $\sigma_1 = 6.57$ and $\sigma_2 = 2.58$. Blue line: horizontal line $Z^* = 0.5$ and $Y^* = 0$. Red line: broken line following the bottom of the vein, 0.5 mm above it at $Y^* = 0$

for cavitation. They thus might be composed of degassed air. The second type of structure consists of an attached cavity in the middle of the vein, just downstream of the throat. It has been observed for $Re \leqslant 800$ and their inception fairly corresponds to the critical value of the cavitation number estimated with numerical simulations. This attached cavity thus probably contains vapor. The third type of structures is reminiscent of the tadpoles and has been called "top tadpoles": they appear for $Re \geqslant 900$ and attach to the upper wall in the secondary boundary layer separation. The pressure in these regions is above the vapour pressure and they might also be composed of degassed air.

In the present Article, with a different protocole of intense degassing at 70 mbars before running the experiments, the bottom and top tadpoles are not observed. This confirms that they are linked to degassing phenomena. Only the central attached cavity remains, and these cavities are moreover observed for cavitation numbers lower than the numerical critical value. The development of these cavities when varying the absolute pressure ate constant Reynolds nuumber, their shape and their temporal features are presented in the following paragraphs.

2.2. Typical case at $Re = 1400$

In this paragraph, data obtained at a Reynolds number $Re \simeq 1410 \pm 10$ are presented and discussed as it is the lower Reynolds number at which all the typical features that have been highlighted are present. Typical instantaneous pictures are shown in Fig. 3. Close to its inception (not shown here), the attached cavity consists of an elongated tiny bubble and covers a width of the order of $h_{throat}/10$. Lowering the cavitation number it first grow laterally and soon reaches a dimensionless width of the order of 0.7. It is then composed of three to four "divots"as can be seen in the first row in Fig. 3. The cavity viewed from side is quite flat and its bottom part is detached from the divergent bottom wall. The cavity is of quite constant length and small gaseous structures detach rapidly in the wake of the cavity, a phenomenon that resembles the diffusion-driven nucleation described in Ref. [14]. This process seems to be intermittent with a typical time scale of the order of 6×10^{-3} s (160 Hz) and the detach structures roll-up in the wake in the shape of hairpin-like vortices.

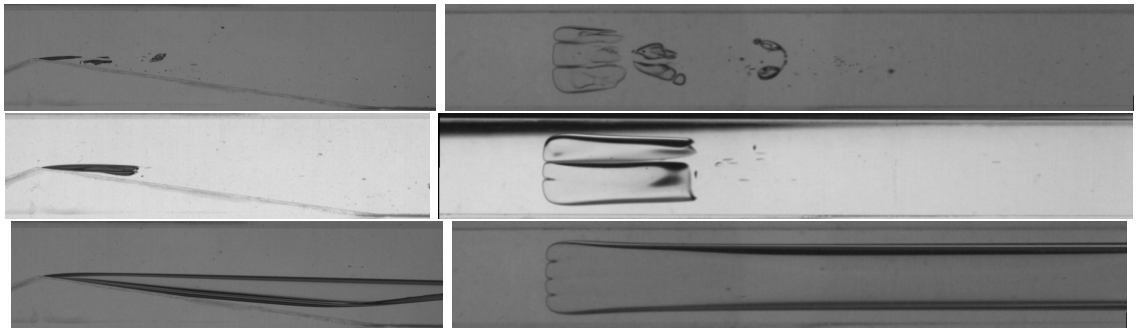

Figure 3. Instantaneous pictures from side view (left column) and top view (right column) at $Re \simeq 1410 \pm 10$. First row: $\sigma_1 = 5.35$, $\sigma_2 = 1.54$; middle row: $\sigma_1 = 5.12$, $\sigma_2 = 1.15$ and last row: $\sigma_1 = 5.03$, $\sigma_2 = 0.34$. See also Fig. 6 to situate these cases in the explored map

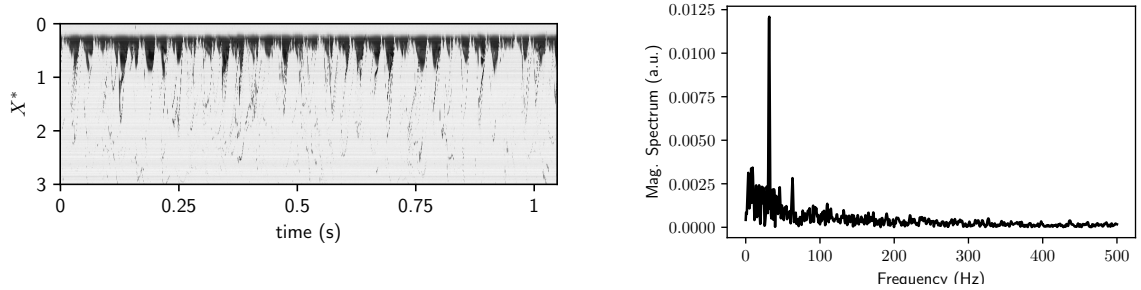

Figure 4. Spatio-Temporal Diagram and corresponding magnitude spectrum along a line parallel to the divergent slope, for the case displayed in the middle row in Fig. 3 ($Re = 1410$, $\sigma_1 = 5.12$, $\sigma_2 = 1.15$)

At lower cavitation numbers (see middle row in Fig. 3), the cavity shape is quite different as its bottom part is closer to the divergent bottom wall (see side view). The rear part of the cavity now periodically shrinks almost up to the throat and a very sharp peak is visible in the time spectra. This phenomenon is illustrated with a spatio-temporal diagram in Fig. 4. One can also notice that the rear part of the cavity is almost vertical.

Finally, for a lower cavitation number, one can obtain a steady cavity that appears to be completely transparent from both top and side view, and whose length is longer than the end of the divergent part of the venturi profile (*i.e.* $X^* \geqslant 7.11$). A picture of it is visible in the third row in Fig. 3. This kind of cavity will be called "supercavity".

Ten data sets obtained at $Re \simeq 1410$ have been analysed. The regimes have been identified and the average length of the cavity has been computed. The dimensionless pressure difference K_p has also been computed. The results are plotted in Fig. 5. When looking at the cavity length as a function of σ_1 (see green + in the left part in Fig. 5), the change in length seems to be extremely abrupt. However, the pressure difference along the experiment depends on the cavity length as can be seen in the right part in Fig. 5. It increases rapidly with the cavity length. The cavitation number based on the outlet pressure σ_2 thus seems to be a more significant parameter to analyse the results. The frequency shedding is observed for cavities of intermediate length, between 1.2 and $4h_{throat}$. The frequency is constant, of the order of 32 Hz in this case.

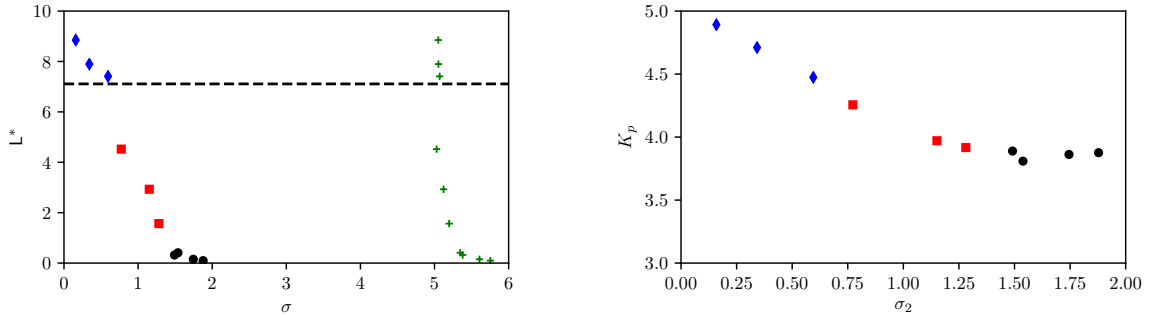

Figure 5. Left: average length of the cavity as a function of the cavitation number. Green +: as a function of σ_1. Other symbols: as a function of σ_2, black circles correspond to type-1 small cavities with no clear periodic shedding, red squares to type-2 cavities with periodic shedding and blue diamonds to supercavities

2.3. Map of the regimes and dependance on the Reynolds number

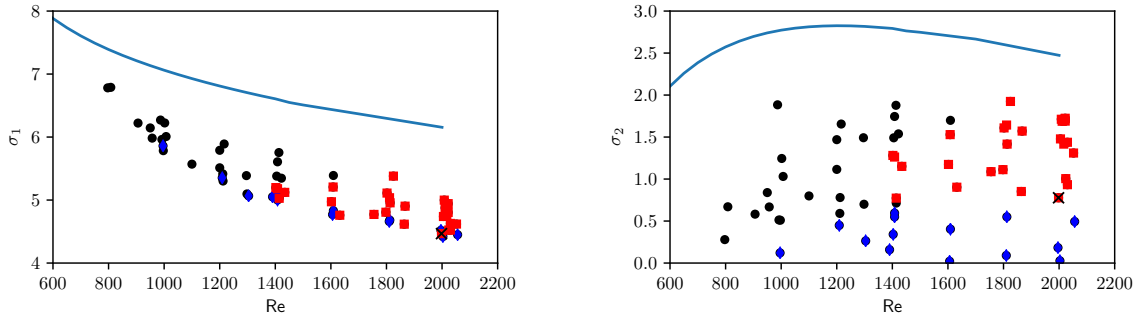

Figure 6. Explored maps in the Reynolds - cavitation number space. Left: data plotted in the $Re-\sigma_1$ space. Right: data plotted in the $Re-\sigma_2$ space. Black circles correspond to type-1 small cavities with no clear periodic shedding, red squares to type-2 cavities with periodic shedding and blue diamonds to supercavities. The solid pale blue line correspond to the critical cavitation numbers obtained with the single-phase numerical simulations

Approximately one hundred of movies have been recorded at various Reynolds numbers and cavitation numbers. Only the cases with no spurious air bubbles coming from upstream and with cavities larger than 1 mm have been reported in Fig. 6. The data all fall below the numerical inception curves. The different regimes seem quite mixed when plotted against the inlet cavitation number σ_1. The regime map is more visible when plotted against the outlet cavitation number.

The type-3 supercavities are observed only for one point at very low pressure at $Re \simeq 1000$ and for higher Reynolds numbers the zone where supercavities are observed progressively extends up to $\sigma_2 \simeq 0.5$. Then, concerning the periodic shedding, none has been observed for $Re \leqslant 1400$. It is present in a narrow range of cavitation numbers $\sigma_2 \in [0.77\ ;\ 1.28]$ at $Re \simeq 1400$ and the extension of this regime then increases for higher Reynolds numbers: for instance it is observed for $\sigma_2 \in [0.72\ ;\ 1.77]$ and could even be present at higher cavitation numbers at $Re \simeq 2000$. The frequency that corresponds to the periodic shedding is plotted as a function of the inlet velocity in Fig. 7. The two quantities are obviously highly correlated.

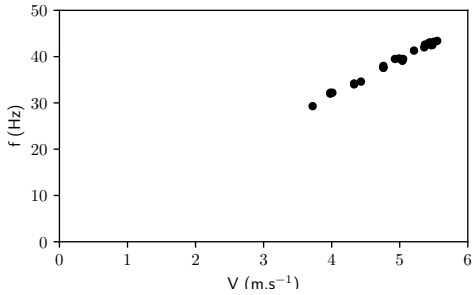

Figure 7. Frequency as a function of the inlet velocity for the periodic shedding cases displayed with red squres in Fig. 6

3. Conclusion

In the present Article, the development of attached cavities under cavitating conditions in a highly degassed silicon oil has been explored. At least three different regimes have been observed: type-1 small cavities that are almost steady, type-2 periodically shrinking cavities of intermediate size, and type-3 supercavities. The regime map in terms of Reynolds and cavitation numbers have been established. The first analysis reveal that the periodic regime appears for a sufficiently great Reynolds number ($Re \geqslant 1400$), first in a narrow range of cavitation numbers and then in a wider range at higher Reynolds numbers. The frequency is almost proportional to the velocity of the upstream flow. More modal analysis with POD or DMD is in progress in order to characterize better this regime. Experiments with higher temporal resolution are needed to characterize other temporal features that are also present such as vortex shedding in the wake of the cavity. Finally, further analysis are in progress in order to characterize the evolution of the length of the cavities with the cavitation number at lower ($Re \simeq 1000$) and higher ($Re \simeq 2000$) Reynolds numbers. Finally, the first results on the supercavities show highly steady divots close to the leading edge of the cavity, with a number of structures that seem to increase linearly with the Reynolds number.

References

[1] Franc J P and Michel J M 2006 *Fundamentals of cavitation* (Kluwer Academic Publishers)
[2] Parkin B R and Kermeen R W 1953 *Clif. Inst. Tech. Hydro. Lab* **Rep. E-35.2**
[3] Arakeri V H 1975 *J. Fluid Mech.* **68** 779–799
[4] Kuiper G 1981 *Cavitation inception on ship propeller models.* Ph.D. thesis Delft University of Technology, Netherlands
[5] Franc J P and Michel J M 1985 *J. Fluid Mech.* **154** 63–90
[6] Guennoun M F 2006 *Étude physique de l´apparition et du développement de la cavitation sur une aube isolée.* Ph.D. thesis EPFL Lausanne, Switzerland
[7] Van Rijsbergen M 2016 A review of sheet cavitation inception mechanisms *16th International Symposium on Transport Phenomena and Dynamics of Rotating Machinery*
[8] Pelz P F, Keil T and Groß T F 2017 *J. Fluid Mech.* **817** 439–454
[9] Callenaere M, Franc J P, Michel J M and Riondet M 2001 *J. Fluid Mech.* **444** 223–256
[10] Ganesh H, Mäkiharju S A and Ceccio S L 2016 *Physics of Fluids* **802** 37–78
[11] Croci K, Ravelet F, Robinet J C and Danlos A 2018 Experimental study of cavitation in laminar flow *Proceedings of the 10th International Symposium on Cavitation (CAV2018)*
[12] Croci K, Ravelet F, Danlos A, Robinet J C and Barast L 2019 *Physics of Fluids* **31** 063605
[13] Danlos A, Ravelet F, Coutier-Delgosha O and Bakir F 2014 *Int. J. Heat and Fluid Flow* **47** 9–20
[14] Groß T F and Pelz P F 2017 *J. Fluid Mech.* **830** 138–164